Earth and Planetary Science Letters 437 (2016) 89–100

Contents lists available at ScienceDirect

Earth and Planetary Science Letters

www.elsevier.com/locate/epsl

Valence and metal/silicate partitioning of Mo: Implications for conditions of Earth accretion and core formation

K. Righter [a,*], L.R. Danielson [b], K.M. Pando [b], G.A. Shofner [c], S.R. Sutton [d,e], M. Newville [d], C.-T. Lee [f]

[a] Mailcode XI2, NASA Johnson Space Center, Houston, TX 77058, United States
[b] JETS, NASA Johnson Space Center, Houston, TX 77058, United States
[c] Department of Physics, Astronomy and Geosciences, Towson University, Smith Hall, Towson, MD 21252, United States
[d] Center for Advanced Radiation Sources, 5640 S. Ellis, Univ. of Chicago, Chicago, IL 60637, United States
[e] Dept. of the Geophysical Sciences, 5734 S. Ellis, Univ. of Chicago, Chicago, IL 60637, United States
[f] Department of Earth Sciences, MS-126, Rice University, Houston, TX 77005, United States

ARTICLE INFO

Article history:
Received 19 October 2015
Received in revised form 17 December 2015
Accepted 20 December 2015
Available online 21 January 2016
Editor: B. Marty

Keywords:
siderophile
core formation
mantle
differentiation
accretion
partitioning

ABSTRACT

To better understand and predict the partition coefficient of Mo at the conditions of the deep interior of Earth and other terrestrial planets or bodies, we have undertaken new measurements of the valence and partitioning of Mo. X-ray absorption near edge structure (XANES) K-edge spectra for Mo have been measured in a series of Fe-bearing glasses produced at 1 bar and higher PT conditions. High pressure experiments have been carried out up to 19 GPa in order to better understand the effect of pressure on Mo partitioning. And, finally, a series of experiments at very low fO_2 conditions and high Si content metallic liquids has been carried out to constrain the effect of Si on the partitioning of Mo between metallic liquids and silicate melt. The valence measurements demonstrate that Mo undergoes a transition from 4+ to 6+ near IW−1, in general agreement with previous 1 bar studies on FeO-free silicate melts. High pressure experiments demonstrate a modest pressure dependence of D(Mo) metal/silicate and, combined with previous results, show a significant decrease with pressure that must be quantified in any predictive expression. Finally, the effect of dissolved Si in Fe-rich metallic liquid is to decrease D(Mo) significantly, as suggested by previous work in metallurgical systems. The effect of pressure, temperature, oxygen fugacity, metallic liquid composition, and silicate melt composition can be quantified by using multiple linear regression of available experimental data for Mo. Our XANES results show that Mo will be 4+ at conditions of core formation, so only experiments carried out at fO_2 of IW−1 and lower were used in the regressions. Application of predictive expressions to Earth accretion shows that D(Mo) decreases to values consistent with an equilibrium scenario for early Earth core–mantle. The Mo content of the primitive upper mantle (PUM) can be attained by metal–silicate equilibrium involving S-, C-, and Si-bearing metallic liquid, and peridotite silicate melt along the peridotite liquidus near 45 GPa and 3600 °C, late in the accretion process. This conclusion is insensitive to late giant impacts unless the degree of equilibration is very low (<5%).

Published by Elsevier B.V.

1. Introduction

Siderophile elements have an affinity for Fe-rich metallic liquids and thus offer information about the conditions of core formation in terrestrial planets. The distribution of siderophile elements (e.g., Fe, Ni, Co, Mo, W) between metal and silicate melt depends upon the variables of pressure, temperature, silicate melt and metal composition, and oxygen fugacity. As such, an understanding of their partitioning behavior can lead to a better understanding of the conditions surrounding the formation of the metallic core of the Earth and other differentiated planetary bodies for which we have samples of their mantles or basaltic crusts.

Molybdenum is an important siderophile element for several reasons: a) it is refractory which means its abundances in the Earth's mantle and building blocks are better known than most elements -23 ± 7 ppb (Greber et al., 2015), b) it is a moderately siderophile element which means its partition coefficient between the core and mantle is a large number, possibly between 10 and 1000, nonetheless leaving a significant concentration in the man-

* Corresponding author.
E-mail address: kevin.righter-1@nasa.gov (K. Righter).

http://dx.doi.org/10.1016/j.epsl.2015.12.025
0012-821X/Published by Elsevier B.V.

tle, c) it has a well-defined depletion in the Earth's primitive upper mantle compared to chondrites, and d) it carries important isotopic anomalies that may result from metal–silicate partitioning and/or nebular heterogeneity and thus understanding the partitioning behavior can help constrain when Mo isotopic signature was established. Despite these attractions, molybdenum partitioning between metal and silicate melt is more difficult to quantify in natural systems due to uncertainties in (1) its valence at high temperature and pressure, (2) the effect of high pressures, and (3) the effect of dissolved light elements (S, C, and Si) in the metallic liquid.

First, Mo can be stable in two oxidation states (4+ and 6+) in silicate melts and the transition between 4+ and 6+ takes place under oxygen fugacity conditions near the IW buffer at 1 bar (e.g., Holzheid et al., 1994; Farges et al., 2006a, 2006b). Although various studies have tried to constrain the valence (Holzheid et al., 1994; Farges et al., 2006a, 2006b; Wade et al., 2012), the approaches are either indirect with large uncertainties based on solubility or D(Mo) metal/silicate (wt% Mo in metal/wt% Mo in silicate) variation with fO_2, or they are based on measurements on FeO-free and/or SiO_2–Na_2O–Al_2O_3 melts at temperatures of 1100 to 1400 °C. Because 4+ or 6+ cation solubility in a silicate melt will be strongly fO_2 dependent, and solubility is linked to the value of D(Mo) metal/silicate, it is very important to know under what conditions Mo is 4+ and/or 6+ and whether that transition occurs at fO_2s that are within the range of core formation especially at the high temperature and pressure conditions at which the core may have formed.

Second, current models predict high PT metal–silicate equilibrium conditions (30 to 70 GPa; 3000–4000 K) to explain Mo content of the mantle, but most experimental data are acquired from experiments at relatively low PT conditions (<10 GPa, <2300 K), especially relative to moderately siderophile elements such as Ni, Co, or W (Cottrell et al., 2009; Kegler et al., 2008). Mo solubility in silicate melts is strongly dependent upon silicate melt structure and composition (e.g., O'Neill and Eggins, 2002). Melt structure can change significantly at higher pressures (e.g., Poe et al., 2001; Sanloup et al., 2013). Therefore, more partitioning data at the high pressures of a deep magma ocean are needed, and a solid understanding of these effects is needed before quantitative and high precision modeling can be undertaken.

Third, Earth's core contains 10 wt% of a light element that might include all or some of C, S, Si, H, O or N (e.g., Hillgren et al., 2000). The effects of C and S are well understood through various previous studies (Siebert et al., 2011; Wade et al., 2012; Jana and Walker, 1997a, 1997b). Because Si has been proposed as a major component of the Earth's core (Armytage et al., 2011; Shahar et al., 2009; Georg et al., 2007; Ziegler et al., 2010; Savage and Moynier, 2013; Fitoussi et al., 2009; Chakrabarti and Jacobsen, 2010; Dauphas et al., 2015), understanding the magnitude of its effect is important. There is an indication that D(Mo) metal/silicate may be strongly dependent upon the Si content of the Fe metallic liquid (Ono-Nakazato et al., 2007; Tuff et al., 2011), but the magnitude of the effect is unclear, with Tuff et al. (2011) reporting a weaker effect than Ono-Nakazato et al. (2007). Additional work on the effect of Si on D(Mo) metal/silicate is important in achieving confidence in the modeling calculations of Mo in the primitive Earth's mantle.

In order to better understand the partitioning behavior of Mo between metal and silicate melt, we have undertaken a study to a) measure the valence of Mo in experimental glasses equilibrated with Fe metal liquid across a wide range of P–T–fO_2 conditions using XANES spectroscopy, b) isolate the effect of pressure on D(Mo) metal/silicate, and c) isolate the effect of Si on D(Mo) metal/silicate. The results were combined with data from previous studies of D(Mo) metal/silicate (Siebert et al., 2011; Wade et al., 2012; Tuff et al., 2011; Hillgren et al., 1996; Walter and Thibault, 1995; Righter et al., 1997; Jana and Walker, 1997a, 1997b; Wade and Wood, 2001; Righter and Drake, 1999; Righter et al., 2010) and then applied to core formation modeling for the Earth.

2. Experiments

2.1. Partitioning experiments

2.1.1. Piston cylinder (1 GPa)

Metal–silicate equilibrium experiments were carried out in a piston cylinder apparatus to investigate the effect of Si (in Fe liquid) on D(Mo) by comparison to Si-free series of Righter et al. (2010) (Tables S1 and S2). Experiments at 1.0 GPa and 1600 °C were conducted using a non-end-loaded piston cylinder apparatus at NASA-JSC. Experimental details of pressure and temperature control, and the assemblies were presented in Filiberto et al. (2008) and Righter et al. (2006). The sample used in this series of experiments was composed of 70 wt% Knippa Basalt, the composition of which is described in Lewis et al. (1993), 29 wt% Fe and 1 wt% MoO_3 (Table S1; Supplementary Information). Addition of Si metal to the mixture resulted in variable amounts of Si in the metallic liquids which in turn resulted in variable fO_2 (see fO_2 section in "Results" below) in the sample. These mixtures were ground to a powder and mechanically mixed again. Graphite capsules were used, and once samples were under pressure, they were heated to silicate superliquidus temperatures, and then equilibrated at 1600 °C. Run durations were chosen based on equilibration times from previous experiments (Righter et al., 2010; Berthet et al., 2009; Table S2). The samples were then power quenched to a silicate glass which contained large metallic liquid spheres (Fig. 1; cow 3 and cow B1).

2.1.2. Multi-anvil

To investigate D(Mo) at high pressure and temperature conditions, where there are fewer experimental data available, we carried out several experiments in a multi-anvil apparatus, between 12 and 19 GPa (Table S2). Run charges were contained in graphite and single crystal MgO capsules (Table S2). Pressure and temperature in the multi-anvil experiments were generated using COMPRES 10/5 and 8/3 assemblies, and calibrated as reported in Righter et al. (2008) and Shofner (2011). The samples were also power quenched to a silicate glass which contained metallic liquid spheres (Fig. 1; GN24). Some of the experimental glasses were used for XANES measurements as well as partitioning studies. The experiments of Shofner (2011) focused on D(W) metal/silicate partitioning, but Mo was added to many of the experimental runs; the metals were analyzed by EMPA (most contained ~0.3 wt% Mo) and reported in the thesis, but the silicates contained Mo concentrations <100 ppm. We have analyzed experiments carried out at 12 to 16 GPa, where sample starting materials consisted of natural peridotite powder (DMP56 and DMP60; Rudnick et al., 2004), mixed with Fe and W metals (Table S1).

2.2. Mo-bearing glass experiments for valence measurements

To create samples with ample Mo contents to measure XANES spectra and determine valences of Mo, we synthesized some Mo-bearing glasses at 1 bar and also elevated pressure. Two compositions were studied at 1 bar and at variable fO_2–ankaramite and basalt (Table S1). The ankaramite series was doped with 500 ppm Mo, whereas the basalt series was un-doped. For the ankaramite series the powder was pressed into a pellet and hung from a Re wire basket, whereas for the basalt (Fig. 1; Mo cow IW−0.5), the pellet was hung from a Re wire loop. Both of these samples were 3

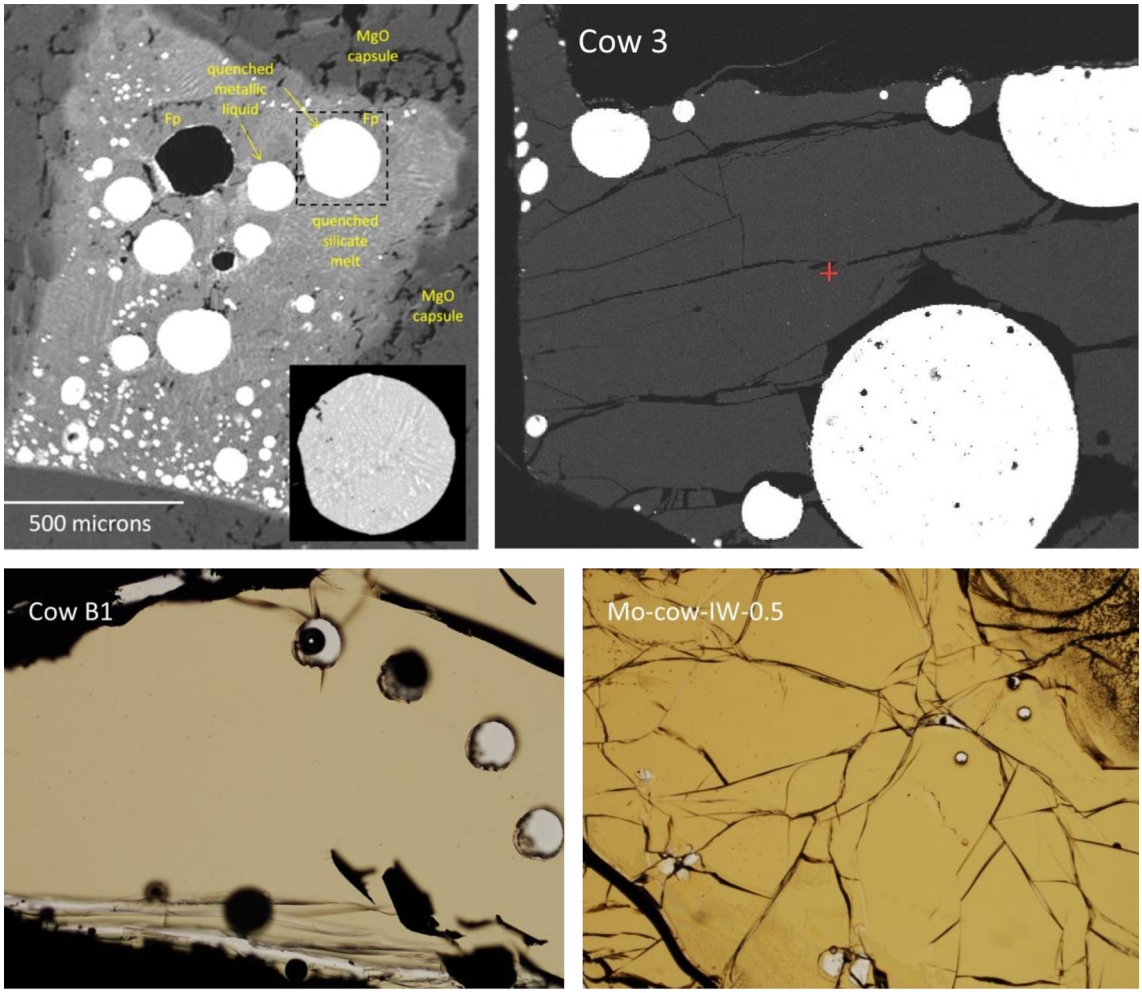

Fig. 1. Examples of typical textures from experimental run products. Top left: Back-scattered electron (BSE) image of experiment GN24 carried out in a multi-anvil apparatus at 16 GPa, 2140 °C with an MgO capsule; scale bar is 500 microns. Top right: BSE image of experiment "cow 3" carried out in a piston cylinder apparatus at 1.0 GPa, 1600 °C with a graphite capsule; width of field of view is 1.1 mm. Bottom left: Plane-polarized light image of experiment "cow B1" carried out at 1.0 GPa, 1600 °C, in graphite capsule at IW−2.5; width of field of view is 2 mm. Bottom right: Plane-polarized light image of 1 bar experiment "Mo-cow IW−0.5" used for Mo XANES measurements and containing 16.5 ppm Mo; width of field of view is 2 mm. Circular features in both bottom images are laser holes created during analysis – the laser ablation analysis was done on thick mounts *before* the thin sections were made.

to 4 mm in diameter, and were equilibrated at 1300 °C for 5 days (120 h). Oxygen fugacity was controlled by mixtures of CO–CO_2 gas and varied from IW+2 to IW−2.8 (Table S2). Glasses were drop quenched into water, thus assuring a quench rate of >500 °C/s. The high pressure glasses were produced in the multi-anvil apparatus at 12 to 24 GPa and 2000 to 2200 °C (Table S2). These experiments included the Knippa basalt (Table S1) doped with 100 ppm Mo contained by a graphite capsule.

2.2.1. Previous experiments

For valence measurements, experiments from several previous studies were used (Table S2). One andesite glass doped with 0.13 wt% MoO_3 was analyzed from Righter et al. (1998), a product that was melted in air (Table S1). This sample was used as a good representative of a Mo^{6+} glass. Righter and Drake (1999) carried out D(Mo) metal–silicate partitioning experiments with hawaiite melts and FeNiMo alloys at 1 GPa, 1300 °C and near IW buffer. These experimental glasses contain low concentrations of Mo from 0.11 ppm to 11.78 ppm by weight (Righter and Drake, 1999). In addition, a series of glasses from piston cylinder experiments of Righter et al. (2010) used a hawaiite silicate composition (Table S1), and were run at higher temperature (1500–1900 °C) and lower fO_2 (IW−1.4). Finally, Righter et al. (2013) carried out experiments on a synthetic shergottite basaltic glass (Table S1) in Mo capsules from 1 to 4 GPa (Mo-1, -2, -2B, -4A, and BJJB-187); these experimental glasses contain appreciable amounts of Mo and allowed Mo valence to be measured at intermediate pressures to some of the other studies at higher and lower pressure.

3. Analyses

3.1. Electron microprobe analysis (EMPA)

Glasses and metals from the run products were analyzed with an electron microprobe for major elements with a CAMECA SX100 electron microprobe, using an accelerating voltage of 20 kV and sample current of 20 to 40 nA (see additional details in Righter et al., 2010). Carbon in metallic phases was analyzed using the standards and approach of Dasgupta et al. (2013), and all elemental abundances were re-calculated using the measured C contents in the matrix corrections. Multiphase quenched silicate melt and metallic melt were analyzed by rastering the beam over a 10 × 10 micron area, for 20 to 50 different regions that were then averaged. Traverses from capsule wall to metal sphere show no variation in composition. Micro-sized metal flakes are visible and were avoided by using BSE imaging. Typical uncertainty for major elements analyzed by the NASA-JSC electron microprobe is <2%,

and for Mo and P in metals <5%. Results of the analyses are presented in Tables S3 and S4.

3.2. Laser ablation inductively coupled plasma mass spectrometry (LA-ICP-MS)

Mo concentrations at very low concentrations (<100 ppm detection limits of EMPA) were obtained by laser ablation inductively coupled plasma mass spectrometry (ICP-MS) at Rice University using ThermoFinnigan Element 2 ICP-MS coupled to a New Wave 213 nm laser ablation system (Agrinier and Lee, 2007). Analyses were performed in medium mass resolution ($m/\Delta m = 3500$) in order to resolve all major isobaric molecular interferences. Isotopes analyzed were both ^{95}Mo and ^{97}Mo (Table S2) for additional assurance that interferences were negligible. Drift of mass calibration was corrected by centering on the $^{40}Ar^{40}Ar^{+}$ dimer in each measurement. The laser was set at 10 Hz pulse frequency and an energy density of 10 mJ/cm^2. Measurements consisted of about 10 analyses of gas flow background followed by 40–50 measurements of the ablation signal. Gas background was averaged and then subtracted from ablation signal. Background-corrected signals were converted to concentrations using a combination of internal and external standards. ^{25}Mg was used as an internal standard for glasses and quenched silicate liquids. USGS basaltic glass standards (BHVO2g, BCR2g) and NIST glasses (610 and 612) were used as external standards for the silicate glasses (Gao et al., 2002; see Table S5, Supplementary Information). Finally, the limit of detection for each analysis was estimated at 3 times the standard deviation of the background divided by the sensitivity of the instrument as monitored by ^{25}Mg (see also Agrinier and Lee, 2007), and uncertainties are typically ~5% of the amount present (1σ). Micro-sized metal flakes are visible and were avoided by using BSE imaging; as with studies of highly siderophile elements, these flakes are common and are interpreted to be present at high PT conditions rather than forming on quench (Malavergne et al., 2016), and so they are avoided during the analyses for Mo. For partition coefficients, this corresponds to a typical uncertainty of 10% (1σ) on the reported values of the partition coefficient; these are the error bars presented in the figures.

3.3. X-ray absorption near edge spectroscopy (XANES)

A monochromatic X-ray beam from a Si(111) double crystal monochromator was focused onto the sample and the fluorescent X-ray yield was plotted as a function of incident X-ray energy (see for example, Sutton et al., 2002). A Vortex ME4 silicon drift energy dispersive detector was used to collect the Mo K fluorescence. Energy calibration was set to 20,000.0 eV for the first derivative peak of the Mo metal foil spectrum. Mo K XANES spectra were typically collected with 3 s dwell times scanning the incident energy (relative to 20,000.0 eV) from −50 to −10 eV in 5 eV steps, −10 to 30 eV in 0.25 eV steps and 2.8 to 9.0 in k (Å^{-1}) in 0.1 steps. The resulting XANES spectra were corrected for detector dead time then normalized so that the below edge intensity was zero and the above edge intensity was unity.

Mo valences were obtained using a linear combination approach based on full XANES spectra. For optimum fitting, end member spectra from the experimental samples were used as standards. The Mo^{6+} standard was the ankaramite IW+2 spectrum whose edge energy was found to match that of MoO_3. We observed two different spectra in the reduced samples with neutral Mo edge positions – because these two components may reflect different neutral coordinations in the glass, we included them both as components in the fits. Two different "cow" spectra were thus used as Mo^0 standards, IW−5 and IW−2.8, with fit results presented as Mo^{0a} and Mo^{0b}, respectively, in Table 1. Both spectra had edge energies similar to that of Mo metal but with distinct detailed structure. The neutral Mo differences may be due to coordination effects, Mo alloying, or possibly grain size effects. The best Mo^{4+} standard was ankaramite IW−2 which had an effective valence of 4.34 based on edge energy comparison with a spectrum of MoO_2. A synthetic Mo^{4+} standard spectrum was produced by subtracting 17% of the Mo^{6+} standard spectrum (ankaramite IW+2). Fits were carried out using Athena (Ravel and Newville, 2005) and the uncertainties in the component weights reported by Athena are its best estimates of the 1 sigma values. Several examples of the results of this linear combination fitting are shown in Fig. 2 and all are presented in Table 1.

The most reduced experiments contained glass with very low concentration of Mo (several ppm) and visible metal flakes. Initial XANES measurements on glassy regions in the thick mounts resulted in a large metal Mo (zero valent) component in the spectra, indicating the likely contribution of the metal flakes to the spectra, and thus a compromised measurement with higher uncertainty. To counter this problem, we prepared thin sections of these reduced problematic samples. The thin sections allowed us to select regions that are visibly free of metallic flakes, not only at the surface (visible with reflected light in the thick mount) but also at depths through the 30 to 50 μm thickness of the sample. The Mo microdistribution in these regions was then mapped by XRF and final analysis spots selected as those isolated from Mo hot spots. XANES analyses of these specially selected spots that are free of interfering metallic flakes yielded much better spectra that were relatively free of the Mo(0) component, and yielded more reliable fits to the Mo^{4+} and Mo^{6+} components that were present. Images and spectra for several of these samples are presented in the Supplementary Information (Figs. S1 to S7), and results presented in Table 1, along with all other results.

4. Results

4.1. Equilibrium and oxygen fugacity

Several lines of evidence can be used to assess whether equilibrium was approached in these experiments. First, if the reaction of metal with silicate did not reach completion or equilibrium, there will be variable silicate compositions according to the equilibrium $2Fe + Mg_2SiO_4 + O_2 = 2MgO + Fe_2SiO_4$ and one might expect to find zoned metal or olivine. However, the silicates and metals are not compositionally zoned, indicating that equilibrium has been attained (see Tables S3, S4). Second, the experiments are very similar in design and duration to experiments of Righter et al. (2010) in which a time series was performed. The duration of the new experiments is longer than the time required for equilibrium defined by these previous experiments (see Table S2). Finally, the experiments reported here are also longer than experiments for which time series have been done for slower diffusing elements such as Mo^{4+} and Mo^{6+} (Righter et al., 1997; Righter and Drake, 1999, 2000).

As mentioned above, Si metal was added to experiments to promote more reduced conditions – Si alloys with Fe at high temperatures, an approach that has been used for example by Berthet et al. (2009) and others to produce a reduced environment in high pressure sample assemblies. An increase in Si content will cause a decrease in fO_2. Oxygen fugacity was calculated relative to the iron-wüstite (IW) oxygen buffer using the expression $\Delta IW = -2 * \log[a_{Fe}/a_{FeO}]$, where a_{Fe} was calculated using the MetalAct program (see Wade and Wood, 2005) and a_{FeO} is calculated according to Holzheid et al. (1997) where $\gamma_{FeO} = 1.6$ for the melts considered in this study. The ΔIW values ranged from ~−1.44 for Si free runs compared to Si bearing runs which produced ΔIW values as low as −5 (Table S2). The range of ΔIW values for these experiments falls in the range considered during Earth's core formation (−1 to −5).

Table 1
XANES measurements from experimental samples.

Sample#	ΔIW	Pressure (GPa)	Mo (ppm)	Temp. (°C)	Mo^6	Mo^4	Mo^{0a}	Mo^{0b}	Effective valence	Non-metal valence
cow B1	−2.5	1.0	0.155	1600	0.000(67)	0.278(75)	0.722(33)	–	1.11(50)	4.00(47)
cow D1	−5	1.0	0.5	1600	0.000(25)	0.499(29)	0.501(12)	–	2.00(19)	4.00(10)
cow1[a]	−1.44	1.0	2.9	1500	0.320(33)	0.015(52)	0.712(119)	0.063(82)	2.64(31)	5.87(29)
cow3[a]	−1.48	1.0	4.2	1600	0.419(47)	0.107(70)	0.457(161)	0.000(114)	3.36(42)	5.56(21)
cow8[a]	−1.45	1.0	4.9	1700	0.536(56)	0.242(79)	0.271(176)	0.000(132)	4.42(49)	5.35(14)
cow20[a]	−1.44	1.0	6	1800	0.271(30)	0.263(51)	0.443(73)	0.000(43)	3.08(28)	4.99(11)
66[b]	−0.72	1.0	11.78	1300	0.325(25)	0.247(38)	0.378(87)	0.091(60)	3.28(23)	5.11(08)
67[b]	−0.84	1.0	0.49	1300	0.184(71)	0.000(82)	0.445(169)	0.403(139)	1.51(56)	5.96(87)
68[b]	−0.72	1.0	0.91	1300	0.232(19)	0.370(26)	0.362(57)	0.077(43)	3.20(16)	4.75(5)
74[b]	−0.70	1.0	3.74	1300	0.101(119)	0.169(124)	0.369(238)	0.365(185)	1.62(89)	4.73(64)
76[b]	−0.69	1.0	4.79	1300	0.158(22)	0.000(32)	0.556(73)	0.320(53)	1.46(20)	5.96(40)
80[b]	−0.66	1.0	8.23	1300	0.119(25)	0.000(41)	0.453(95)	0.500(62)	1.13(24)	5.96(67)
83[b]	−0.63	1.0	4.61	1300	0.456(15)	0.204(23)	0.348(53)	0.019(35)	3.86(14)	5.35(5)
87[b]	−0.68	1.0	0.11	1300	0.190(25)	0.000(41)	0.506(93)	0.317(63)	1.61(24)	5.96(42)
BJJB 126	−1	16.0	108.3	2100	0.000(19)	0.553(27)	0.483(63)	0.023(45)	2.67(17)	4.00(7)
BJJB 127	−1	16.0	∼100	2100	0.000(17)	0.259(25)	0.538(59)	0.264(40)	1.54(15)	4.00(13)
BJJB 130	−1.5	24.0	∼100	2200	0.000(28)	0.425(41)	0.508(96)	0.079(68)	2.18(25)	4.00(13)
BJJB 134	−1	24.0	∼100	2100	0.058(21)	0.608(34)	0.382(81)	0.000(54)	3.14(20)	4.17(6)
BJJB 184	−1.5	12.0	∼100	2000	0.036(22)	0.552(34)	0.511(78)	0.000(53)	2.90(20)	4.12(7)
BJJB 185	−1.5	19.0	279.4	2100	0.000(25)	0.531(42)	0.523(95)	0.021(64)	2.26(24)	4.00(9)
Mo cow IW 0.5	0.5	0.0001	89.3	1300	0.627(64)	0.369(112)	0.000(153)	0.014(87)	5.27(61)	5.23(13)
Mo cow IW	0	0.0001	64.7	1300	0.456(31)	0.477(43)	0.000(93)	0.126(71)	4.62(27)	4.96(6)
Mo cow IW−0.5	−0.5	0.0001	16.5	1300	0.000(61)	0.712(68)	0.288(30)	–	2.85(45)	4.00(17)
Mo cow IW−1.5	−1.5	0.0001	1.6	1300	0.000(75)	0.625(85)	0.375(37)	–	2.50(56)	4.00(23)
Mo cow IW−2.8	−2.8	0.0001	19.7	1300	0.055(9)	0.676(14)	0.269(4)	–	3.03(8)	4.15(2)
Ank IW+2	2	0.0001	13,742	1300	0.981(95)	0.018(11)	0.000(40)	0.000(34)	5.86(10)	6.00(5)
Ank IW+1	1	0.0001	6905	1300	0.963(9)	0.023(13)	0.000(31)	0.000(21)	5.83(8)	5.91(3)
Ank IW	0	0.0001	3160.7	1300	0.969(30)	0.038(51)	0.001(73)	0.000(43)	5.93(28)	5.88(10)
Ank IW−1	−1	0.0001	4479	1300	0.623(15)	0.381(20)	0.063(45)	0.000(34)	5.29(13)	5.21(3)
Ank IW−2	−2	0.0001	722.3	1300	0.172(25)	0.719(35)	0.105(76)	0.054(56)	4.00(22)	4.38(5)
mo-1[c]	0.5	1.0	n.d.	1400	0.611(13)	0.000(18)	0.154(43)	0.274(30)	3.78(11)	5.96(6)
mo-2[c]	0.5	1.5	n.d.	1400	0.000(38)	0.441(57)	0.420(133)	0.202(93)	2.16(34)	4.00(17)
mo-2B[c]	0.5	1.5	n.d.	1400	0.51(19)	0.257(35)	0.152(52)	0.161(30)	3.86(19)	5.25(6)
mo-4A[c]	0.5	3.0	n.d.	1500	0.246(27)	0.000(38)	0.475(83)	0.314(62)	1.91(23)	5.96(30)
BJJB 187	0.5	4.0	n.d.	1600	0.105(16)	0.000(25)	0.453(59)	0.475(40)	1.05(15)	5.96(47)

Samples from previous studies: [a] – Righter et al. (2010); [b] – Righter and Drake (1999); [c] – Righter et al. (2013); n.d. = not determined; Mo^6, Mo^4, and Mo^{0a} and Mo^{0b} are the fraction of each species from the fit, and the "a" and "b" are the two reduced components observed in the spectra (see text for further discussion).

4.2. Glass and metal elemental compositions

The Fe-rich metallic liquid contained between 0.8 and 5.2 wt% Mo, in addition to Fe. In the series with variable Si content, the metallic liquids contained as much as 7.2 wt% Si ($X_{Si} = 0.13$; Table S3). Carbon contents ranged from 2.8 to 6.2 wt%; carbon is lower in the Si-bearing metallic liquids because in the Fe–Si–C system the FeSi-rich liquids contain less C than Fe-rich liquids in the Fe–C system.

The glasses produced are typically basaltic glasses with 11.7 to 23.2 wt% MgO and 40 to 50 wt% SiO_2 (Tables S3 and S4). FeO contents are variable with fO_2; the lowest fO_2 experiments (Cow D and C; Table S3) contain ∼0.1 wt% FeO, whereas the higher fO_2 experiments contain as much as 13.3 wt% FeO (Table S4). The Mo contents of the glasses are also variable with doping levels and oxygen fugacity. The Mo solubility ankaramite glasses contain from 700 to 13,700 ppm of Mo – these melts were doped with Mo and equilibrated with Re wire and thus had higher final Mo contents. The Mo solubility basalt series was un-doped, equilibrated at variable fO_2 and contained 1.6 to 90 ppm Mo. In each series the highest Mo contents were measured in the highest fO_2 of equilibration (>IW; Table S2). In the 1 GPa partitioning experiments, Mo contents of the glasses were lowest in the low fO_2 experiments, 0.2 to 0.5 ppm, compared to the higher fO_2 runs in which Mo contents were >4.0 ppm (Tables S1, S2 and Righter et al., 2010). In the BJJB multi-anvil experiments, Mo contents were considerably higher, and ranged from 100 to 185 ppm. And, for the GN series multi-anvil experiments (from Shofner, 2011), Mo contents are between 34 and 90 ppm (Table S2).

4.3. Glass valences

Examination of the effective valence in many of the results from this study shows that many of the samples exhibit evidence for lower valence than 4 (Table 1). Although it is possible that lower valences exist, we attribute this effect to the possibility of interfering metal flakes in the silicate melts. Because Mo has a very low solubility in silicate melts, Mo metal saturates in silicate melt very easily. In some samples there are metal flakes present and in many of the run products the metal undoubtedly interferes with the XANES analyses of the glass. Because Mo^0, Mo^{4+} and Mo^{6+}, all have distinct spectral features, each spectrum can be fit with a linear regression, to determine what proportion of each species is represented (see previous XANES methods section). When the contribution of interfering metal flakes are subtracted from the overall spectrum, the Mo^{6+} to Mo^{4+} contents, or "non-metal" valence, can be determined. These are shown in Fig. 3.

4.4. Partition coefficients

The very low solubilities of Mo in the glasses from the series of partitioning experiments with Si-bearing metal result in very high partition coefficients for Mo. Values range from 270 to 7200 in the Si-free samples to 34,000 to 137,400 in the Si-bearing samples. For the high pressure experiments, D(Mo) ranges from 96 to 250 (Table S2).

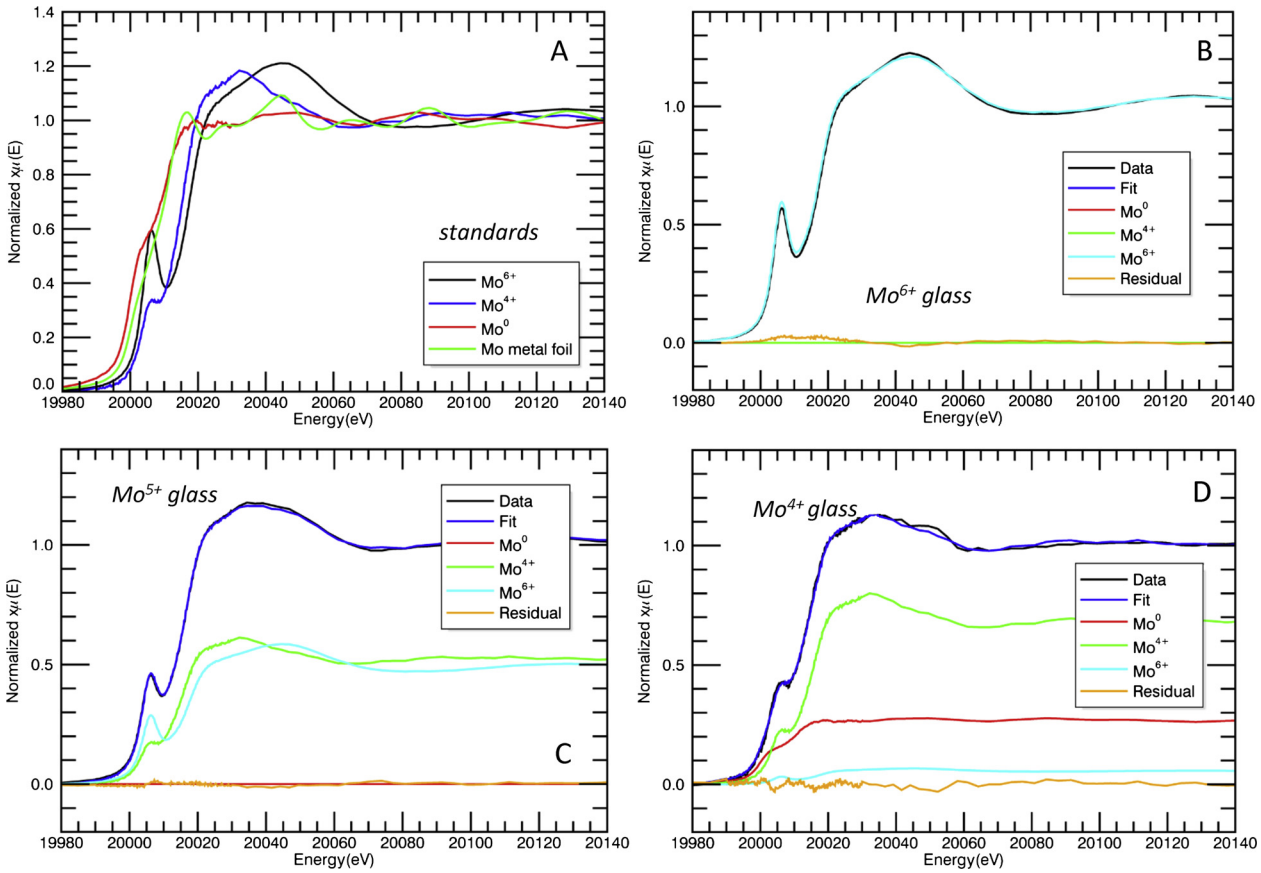

Fig. 2. (a) Mo K XANES spectra (normalized) for the standards used in the linear combination fitting for valence determinations. Mo^{6+} is the spectrum for the ankaramite IW+2 glass. Mo^{4+} is the ankaramite IW−2 glass corrected for 17% Mo^{6+} indicated by comparison with spectra for MoO_2 and MoO_3. Mo^0 is the measured spectrum for metal nuggets in the cow IW−2.8 sample. Mo metal foil, shown for reference only, is an energy calibration foil (EXAFS Materials, Danville, CA) collected in transmission. (b) Mo K XANES spectrum for ankaramite IW+1 (black), the linear combination fit (blue) and the component fits for the three valence standards: Mo^0 (red; 0%), Mo^{4+} (green; 0%), and Mo^{6+} (cyan; 100%). The residual from the fit is shown in orange. The valence for the non-metal component was dominantly 6.0 (5.91 in Table 1). (c) Mo K XANES spectrum for ankaramite IW−1 (black), the linear combination fit (blue) and the component fits for the three valence standards: Mo^0 (red; 0%), Mo^{4+} (green; 51%), and Mo^{6+} (cyan; 49%). The residual from the fit is shown in orange. The valence for the non-metal component was a nearly equal mixture of 4 and 6 (5.21 in Table 1). (d) Mo K XANES spectrum for COW IW−2.8 Spot 2 (black), the linear combination fit (blue), and the component fits for the three valence standards: Mo^0 (red; 27%), Mo^{4+} (green; 68%), and Mo^{6+} (cyan; 5%). The residual from the fit is shown in orange. The valence for the non-metal component was dominantly 4.0 (4.2 in Table 1).

5. Discussion

5.1. Valence–effect of fO_2 and elevated pressure and temperature

After the effect of metallic Mo is corrected, the "non-metal" valence can be re-examined for systematic behavior. In particular the transition from Mo^{6+} to Mo^{4+} can be studied. Considering only those spectra from 1 bar glasses where the metal contributions were less than 50% (i.e., where there is higher reliability in fitting the non-metal component), one can see that there is a fairly nice trend transitioning between 6+ and 4+ over about 3 orders of magnitude centered at about IW−0.5 (Fig. 3a). Thus, the transition from Mo^{6+} to Mo^{4+} occurs largely between IW and IW−1, in good agreement with the 1 bar studies of Holzheid et al. (1994) and O'Neill and Eggins (2002), who concluded Mo changed dominant valence from Mo^{6+} to Mo^{4+} at around IW−1 (Fig. 3a). Calculation of a hypothetical transition of Mo from 4+ to 6+ centered at IW−0.5 and based on the 2-electron transition of $Mo^{4+}O_2 + 1/2O_2 = Mo^{6+}O_3$, results in a curve that closely corresponds to our data in this fO_2 range (Fig. 3b). At the conditions of core formation, near IW−2, Mo^{6+} is present only at trace levels. Farges et al. (2006a) suggested Mo^{5+} may be stable around IW, but Farges et al.'s (2006a) evidence for stable Mo^{5+} (determined from additional electron paramagnetic resonance spectroscopy data) appears only in FeO-free systems. It is thus more likely that we have a mixture of Mo^{4+} and Mo^{6+} across a small fO_2 range, yielding to predominately Mo^{4+} at IW−2 and below. In addition, there may be quench effects involving redox couples such as have been observed for Cr and Fe in experimental studies (Berry and O'Neill, 2004). In that experiment, the reaction $Cr^{2+} + Fe^{3+} \rightarrow Cr^{3+} + Fe^{2+}$ was hypothesized to be operating at IW+2 causing oxidation of Cr^{2+} to Cr^{3+} during quench. In our experiments, it is possible that the reaction $Fe^{3+} + Mo^{4+} \rightarrow Fe^{2+} + Mo^{6+}$ could have operated during quench, causing oxidation of Mo^{4+} to Mo^{6+}, but at IW there is very little Fe^{3+} stable in FeO-bearing melts (Righter et al., 2013); in the ankaramite series, for example, the Mo contents range from 700 to 14,000 ppm Mo, much higher than Fe^{3+} expected at these low fO_2 conditions. Nonetheless oxygen fugacity of the Mo^{4+} to Mo^{6+} transition determined in the present study can be considered a conservative lower limit.

The measurements made on high pressure and high temperature glasses indicate that Mo^{4+} is dominant at oxygen fugacity below IW−1 (Fig. 4). At temperature between 1500 and 1800 °C, Mo valence is lowered from 6 to <5, and then at 2000 to 2200 °C, the valence is 4 (Fig. 4a). High pressure glasses between 12 and 24 GPa and IW−1.5 exhibit a valence of 4, whereas lower pressure glasses at IW+0.5 contain Mo dominated by valence of 6 (Fig. 4b). Note that experiment Mo-2 yielded Mo^{4+} spectrum at 1 GPa, but this experiment contained small crystals of MoO_2 and the spectrum for this glass had a strong resemblance to MoO_2, leading us

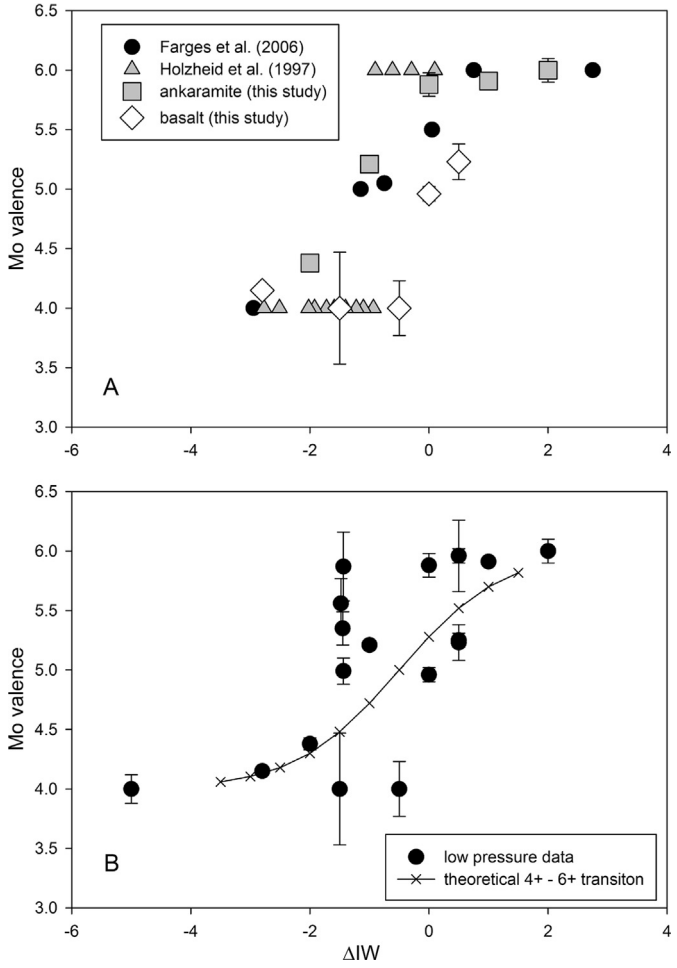

Fig. 3. Top: Comparison of ankaramite and basalt series (1 bar) to those of Holzheid et al. (1994) and Farges et al. (2006) showing relatively narrow range where all studies, regardless of temperature or melt composition, undergo transition from Mo^{4+} to Mo^{6+}. Bottom: Plot of non-metal valence versus relative fO_2 (ΔIW) for the low-pressure subset of samples from this study – shown are those at 1 bar and 1.0 GPa only. The curve shows the expected (theoretical) width of the two electron transition $Mo^{4+} = Mo^{6+} + 2e^-$ centered on IW−0.5, which correlates well with our data in this fO_2 range. The shape of the curve is determined by the stoichiometry of the redox reaction $Mo^{4+}O_2 + 1/2O_2 = Mo^{6+}O_3$, and is a function of the power to which fO_2 is raised (−1/2), for a two electron reaction. The non-metal valence data points shown (filled circles) are for analyses with small metal flake components after correction for those components (see text).

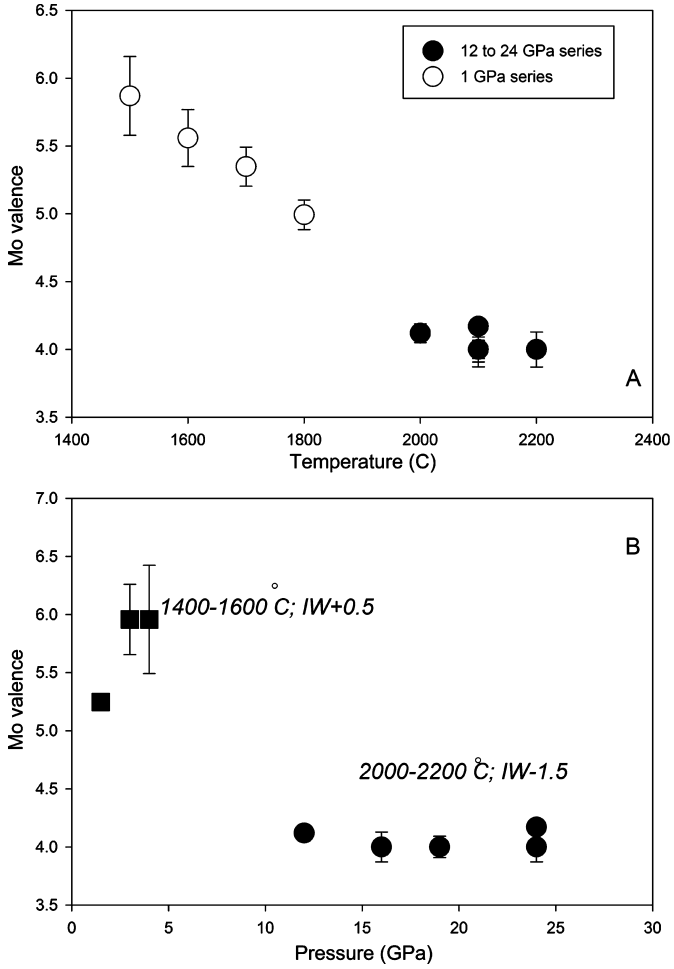

Fig. 4. Plot of non-metal valence versus temperature and pressure. High PT experimental results indicate that as temperature increases from 1500 to 1800 °C, Mo valence decreases from 6 to 5, and then at the high temperatures of 2000 to 2200 °C, a valence of 4 is dominant. At pressures between 12 and 24 GPa and IW−1.5, Mo exhibits a valence of 4. Between 1 and 4 GPa and IW+0.5, Mo exhibits dominantly 6+ valence. Experiment Mo-2 is not plotted with this series because its spectrum looked similar to that of MoO_2 and small MoO_2 crystals were present in the glass in this experiment.

to the conclusion that this sample should be omitted from the glass valence assessments. There is no particular correlation between Mo content of glass and valence with the exception of the ankaramite series in which the Mo contents increase with valence due to the increasing solubility of Mo in equilibrium with the Mo foil at higher fO_2s. The main factor in determining valence is oxygen fugacity.

5.2. Effect of Si in Fe metal

The effect of Si on Mo partitioning between metal and silicate can be examined using four experiments from this study (cow B1, C2, D1, 3), coupled with the Fe exchange coefficient K_d(Fe–Mo) based on the equilibrium:

$$2Fe + MoO_2 = 2FeO + Mo \quad (1)$$

This equilibrium is independent of oxygen fugacity, and therefore can be used to isolate the effect of Si on Mo partitioning. Consider that

$$\ln K = \ln \frac{[a^{metal}_{Mo}][a^{silicate}_{FeO}]^2}{[a^{silicate}_{MoO_2}][a^{metal}_{Fe}]^2} = \ln \frac{[X^{metal}_{Mo}][X^{silicate}_{FeO}]^2}{[X^{silicate}_{MoO_2}][X^{metal}_{Fe}]^2} + \ln \frac{[\gamma^{metal}_{Mo}][\gamma^{silicate}_{FeO}]^2}{[\gamma^{silicate}_{MoO_2}][\gamma^{metal}_{Fe}]^2} \quad (2)$$

where a refers to activity, X refers to mole fraction, and γ refers to the activity coefficient. We set $K_D = \frac{[X^{metal}_{Mo}][X^{silicate}_{FeO}]^2}{[X^{silicate}_{MoO_2}][X^{metal}_{Fe}]^2}$ and assume the ratio of oxide activity coefficients in the silicate, $\frac{[\gamma^{silicate}_{FeO}]^2}{[\gamma^{silicate}_{MoO_2}]}$, is fixed, since in this series the silicate melt composition is nearly constant from experiment to experiment (see expts. cow-B1, -C2, -D1, and -3 all with $(MgO + CaO)/(SiO_2 + Al_2O_3)$ values between 0.55 and 0.7). On the other hand, the metal composition varies significantly in Si content and the ratio of activity coefficients in the metal, $\frac{[\gamma^{metal}_{Mo}]}{[\gamma^{metal}_{Fe}]^2}$, is dependent upon variations in metal composition. Then equation (2) above can be re-arranged to yield $\ln K_D = \text{const} + 2\ln\gamma^{metal}_{Fe} - \ln\gamma^{metal}_{Mo}$. And when combined with $\ln\gamma^{metal}_{Mo} = \ln\gamma^{metal}_{Fe} + \ln\gamma^{0}_{Mo} - \varepsilon^{Si}_{Mo}\ln(1 - X_{Si})$ yields:

$$\ln K_D - \ln\gamma^{metal}_{Fe} = \text{const} - \ln\gamma^{0}_{Mo} + \varepsilon^{Si}_{Mo}\ln(1 - X_{Si}), \quad (3)$$

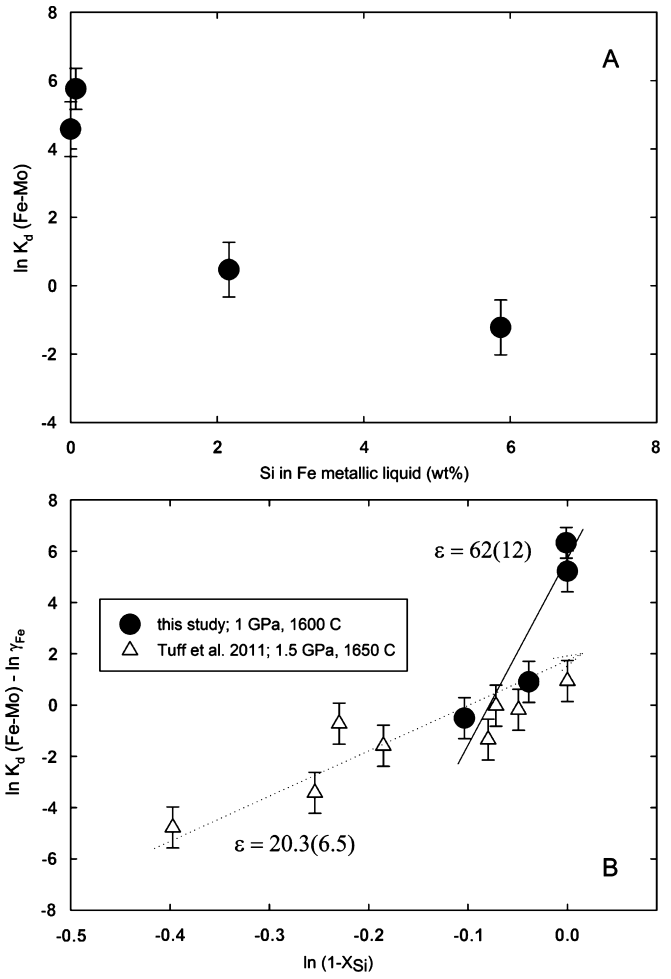

Fig. 5. (a) $\ln K_d$(Fe–Mo) vs. Si content of the metallic liquid showing the decrease at higher Si contents. (b) $\ln K_d$(Fe–Mo)/γFe vs. $\ln(1 - X_{Si})$, the slope of which yields the interaction parameter ε^{Si}_{Mo}. Plotted are three new experiments from this study, cow B1, C2, and D1, as well as one Si-free experiments from Righter et al. (2010) at the same temperature – all at 1600 °C. For comparison are the results for Mo reported by Tuff et al. (2011) at 1650 °C, 1.5 GPa in MgO capsules. The C-undersaturated or C-free experiments yield a lower value of ε^{Si}_{Mo} than those from the C-saturated series.

where ε^{Si}_{Mo} refers to the interaction parameter for Mo in Si alloyed with Fe (Wagner, 1962; Wade and Wood, 2005; Ma, 2001; Wood et al., 2014).

The slope of $\ln K_D - \ln \gamma^{metal}_{Fe}$ versus $\ln(1 - X_{Si})$ gives ε^{Si}_{Mo} directly (Fig. 5). Slopes were determined by linear regression using SigmaStat 12.0. The resulting value of 62(±12) is in agreement with the previous work of Ono-Nakazato et al. (2007), whose value is 43(±13), but higher than reported by Tuff et al. (2011) whose value is 22(±5). This difference may be due to the presence of C in our experiments and those of Ono-Nakazato et al. (2007), compared to the C-free experiments of Tuff et al. (2011). Even though several of our points fall along the trend of Tuff et al. (2011), the two points at very low Si content (but significantly different C content) show an important effect of C, therefore these two data sets should not be combined; the overlap in our two points is coincidental. The effect of Si is to reduce the $\ln K_d$(Fe–Mo) from values near 6 to as low as −2 (Fig. 5). This magnitude of reduction is important to quantify and is larger than the effect of S or C on Mo partitioning documented in previous work (e.g., Jana and Walker, 1997a, 1997b; Righter and Drake, 1999). The value of epsilon can be used as an indicator of the effect of S on activity coefficient, and for comparison the recent work of Wood et al. (2014) measured $\varepsilon^{S}_{Mo} = 2.27$. Because the Earth's core was not C-saturated we use the value $\varepsilon^{Si}_{Mo} = 22$ in all of our subsequent modeling.

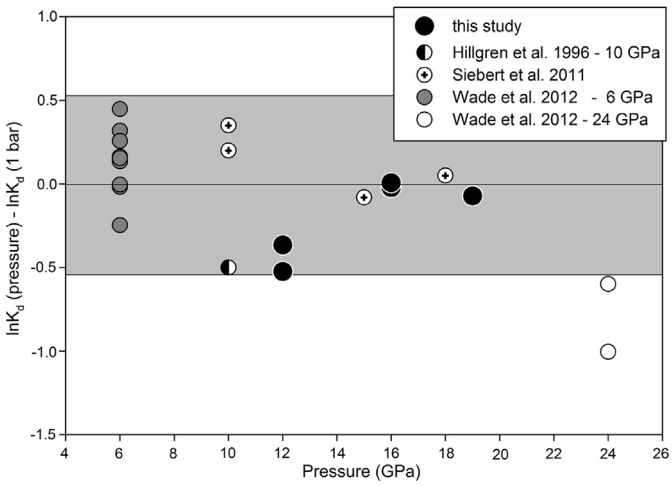

Fig. 6. $\ln K_d$(Fe–Mo) vs. pressure for our experiments compared to those of Wade et al. (2012) at 6 and 24 GPa, as well as Hillgren et al. (1996) at 10 GPa, and Siebert et al. (2011) at 15 and 19 GPa. None of the metallic liquids in these experiment contain Si. Shaded grey region is the standard error on the regression of 1 bar data.

5.3. The effect of pressure

The effect of pressure can be examined combining our results with previous high pressure experiments – above and below the pressures of our study. As with the examination of the effect of Si, the use of K_d(Fe–Mo) instead of D(Mo) will eliminate any variation that is due to different fO_2 of the experiments being compared. When the $\ln K_d$(Fe–Mo) from these experiments are plotted versus pressure, it is clear that pressure causes a slight decrease in $\ln K_d$(Fe–Mo), on the order of one $\ln K_d$ units at 25 GPa (Fig. 6). Our data are consistent with the trend defined by previous works of Hillgren et al. (1996), Siebert et al. (2011) and Wade et al. (2012). Our new results double the number of experimental data available for Mo at pressure >10 GPa.

5.4. Prediction of D(Mo) met/sil

To predict the metal–silicate partitioning of Mo for application to Earth, we will use the partition coefficient, or D, approach based on a simple metal-oxide equilibrium:

$$Mo + O_2 = MoO_2 \quad (4)$$

Considering that $\Delta G = -RT \ln K$, and expanding the free energy term to $\Delta H - T\Delta S + P\Delta V = -RT \ln K$, and the equilibrium constant to $K = (aMO_{x/2})/(aM)(fO_2) = (\gamma MO_{x/2} * xMO_{x/2})/(\gamma M * xM)(fO_2)$. And recombining equals $-\Delta H/RT + \Delta S/R - P\Delta V/RT = \ln[(\gamma MO_{x/2} * xMO_{x/2})/(\gamma M * xM)(fO_2)] = \ln(\gamma MO_{x/2}) - \ln \gamma M + \ln xMO_{x/2}/xM - \ln fO_2$. Rearranging yields:

$$\ln(xM/xMO_{x/2}) = (\Delta H/R)/T - \Delta S/R - +(\Delta V/R)P/T_- \ln fO_2 + \ln(\gamma MO_{x/2}) - \ln \gamma M, \quad (5)$$

and substituting $D(M) = xM^{metal}/xMO^{silicate}_{x/2}$, the expression becomes:

$$\ln D(M) = a \ln fO_2 + b/T + cP/T + \ln(\gamma MO\gamma) - \ln \gamma M + \text{const}. \quad (6)$$

Using this approach, and incorporating silicate liquid compositional term nbo/t as a proxy for the activity coefficient of species M in silicate melt, $\ln(\gamma MO_{x/2})$, equation (6) becomes:

$$\ln D(\mathrm{M}) = a \ln fO_2 + b/T + cP/T + \mathrm{d}(\mathrm{nbo/t}) + e + \ln \gamma(\mathrm{M})_{\mathrm{met}} \quad (7)$$

$$\ln D'(\mathrm{M}) = \ln D(\mathrm{M}) - \ln \gamma(\mathrm{M})_{\mathrm{met}} = a \ln fO_2 + b/T + cP/T + \mathrm{d}(\mathrm{nbo/t}) + e \quad (8)$$

Constants a through e can be derived by multiple linear regression of existing experimental data. Equation (4) is clearly dependent upon fO_2, and so is most effectively applied when the valence is constant. Again, this can be used as long as the valence is dominantly 4, and thus using experiments that were equilibrated at <IW−1. fO_2 is calculated using the IW buffer of Campbell et al. (2009) along with activity of Fe using MetAct (Wade and Wood, 2005; Ma, 2001) and activity coefficient of FeO in silicate melt (as explained above).

Datasets used in the regression include 155 experiments and are: 10 new experiments from this study, 35 experiments from Siebert et al. (2011) between 1.5 and 18 GPa, 1600 to 2600 °C, and C-bearing metals; 46 experiments from Wade et al. (2012) between 1.5 and 24 GPa, 1475 to 2450 °C, ΔIW = −0.9 to −3.4; 20 experiments from Tuff et al. (2011) at 1650 to 1850 °C, 1.5 to 6 GPa and with variable Si in metallic liquids; 10 experiments from Righter et al. (2010) at 1 GPa, 1500 to 1900 °C and variable silicate melt compositions, 2 experiments from Hillgren et al. (1996) and 10 GPa, and 2000 °C; 14 experiments from Walter and Thibault (1995) 1800 to 2400 °C, and 1 to 7 GPa with C-bearing metallic liquids; 13 experiments from Righter et al. (1997) and Righter and Drake (1999) at 1 GPa and 1300 °C, 2 experiments from Jana and Walker (1997a, 1997b) at 8 GPa, 2300 °C; and 3 experiments from Wade and Wood (2001) at 25 GPa and 2300 °C. Altogether there are 155 experiments utilized covering 1 to 25 GPa, 1300 to 2600 °C, ΔIW = −1 to −6.8, S-, C-, and Si-bearing metallic liquids, and basaltic to peridotitic silicate melt. The result of the regression is shown in Fig. S10 (Supplementary Information) and regression coefficients presented in Table S6. The uncertainties on each coefficient are measures of the precision of the estimates of the regression coefficients. Traditional statistical tests such as R^2 (coefficient of determination), t values, P values, and F statistics are used to evaluate the quality of the regressions and the significance of each term. Derivation of an fO_2 coefficient (a) value near −1 indicates that Mo is dominantly 4+ ($a = -1.5$ would indicate 6+), which is consistent with our XANES results. The pressure term in the regression is consistent with the magnitude of the effect in Fig. 6. The effect of C dissolved into the metallic liquid is to increase $\ln D$(Mo), whereas the effect of dissolved S and Si is to decrease $\ln D$(Mo). The effect of Si is much stronger than the effect of S. The melt compositional terms are in agreement and in general show increase in $\ln D$(Mo) with higher Si and Al content and a decrease in $\ln D$(Mo) higher Mg or Ca contents. We will now consider application of these expressions to the Earth's mantle.

6. Application to Earth

6.1. Defining the D(Mo) and K_d(Fe–Mo) required for core–mantle equilibrium

Using geochemical data and estimates for the core and mantle Fe and Mo compositions, K_d(Fe–Mo) and D(Mo) required to explain the upper mantle Mo content by metal–silicate equilibrium can be calculated. Using Fe and FeO content of core and mantle (85.5 wt% and 8.0 wt%, respectively; McDonough, 2003) and Mo content of core and mantle (5 ppm and 27 ppb, respectively; McDonough, 2003; Greber et al., 2015), $\ln K_d$(Fe–Mo) (molar) required to explain the FeO and MoO_2 content of primitive mantle is 0.17 ($\ln K_d$(Fe–Mo) = −1.71). Similarly, using the Mo content of upper mantle 27 ppb; and Mo estimate for the core (based on mass balance and assuming a range of chondrite compositions from CI to EH; Newsom, 1995), required D(Mo) is ~60 to 120. These values will be used in detailed modeling presented below.

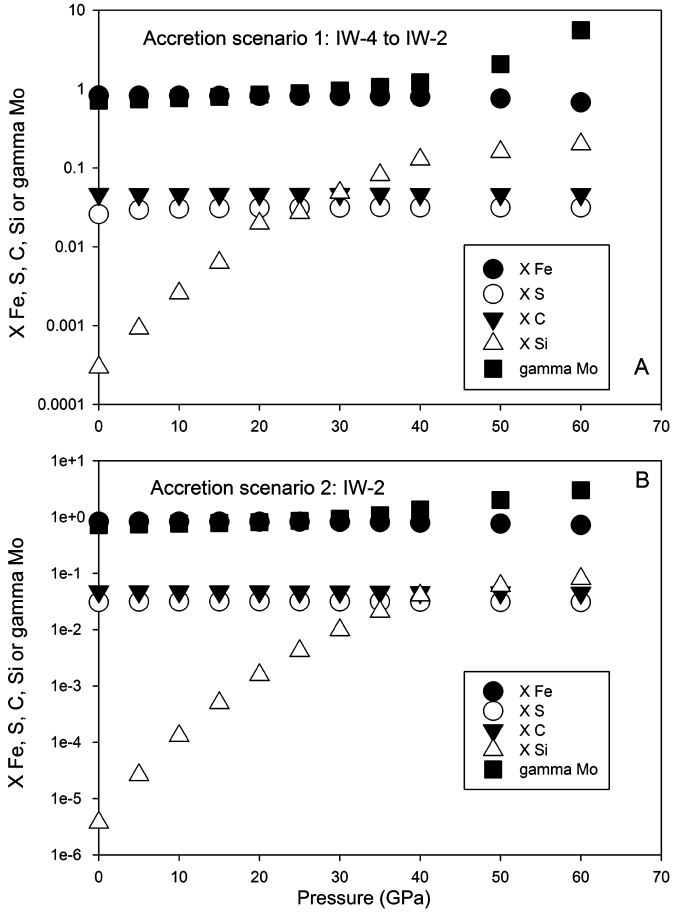

Fig. 7. Comparison of Fe, S, C, and Si content of the core-forming metallic Fe liquid as accretion proceeds for two different fO_2 paths during accretion: a) one which starts reduced (IW−4) and finishes more oxidized (IW−2), and b) one which is relatively constant (IW−2). Pressure is along an adiabat as described in the text, and the S, C, and Si contents of the metallic liquid are calculated according to Boujibar et al. (2014), Chi et al. (2014), and Ricolleau et al. (2011).

6.2. Calculation of D(Mo), D'(Mo), and [Mo] in mantle as Earth accretes

Recent magma ocean modeling indicates moderately siderophile element depletions in Earth's primitive upper mantle can be explained by metal–silicate equilibrium between metallic and silicate liquid at high PT conditions during Earth's accretion (~40 GPa, ~3600 °C; e.g., Righter, 2011; Wade et al., 2012; Siebert et al., 2011). There is some debate about the specific PT conditions, and whether the oxygen fugacity in the mantle changed during accretion or was relatively constant. Modeling suggests that fO_2 started low and eventually became higher during accretion (e.g., Wood et al., 2006; Rubie et al., 2011), whereas some recent calculations indicate that fO_2 may have decreased (Badro et al., 2015; Siebert et al., 2013) or changed only slightly during accretion (Righter and Ghiorso, 2012). If the oxygen fugacity is changing during accretion, the core forming metallic liquid will also change because reduced conditions will favor Si dissolution, whereas oxidized conditions will favor S or C. These light elements will exert a strong effect on the activity coefficients of each trace metal as we have seen in this study and discussed above.

Due to this uncertainty in the fO_2 evolution of the growing Earth, we examine the evolution of the composition of the Earth's

PUM during continuous accretion considering two scenarios: one with nearly constant fO_2 (IW−2) and one with increasing fO_2 (IW−4 to IW−2). The core metallic liquid S, C, and Si composition is calculated according to the studies of Boujibar et al. (2014), Chi et al. (2014), and Ricolleau et al. (2011), respectively (Fig. 7). Calculations have been carried out along the PT conditions of the liquidus for peridotite, according to Andrault et al. (2011). Equilibration between metal and silicate in Earth occurs instantaneously so that as the Earth grows there is constant re-equilibration between the core and mantle (e.g., Deguen et al., 2014; Kendall and Melosh, 2014). The equation used to calculate mantle Mo concentrations is:

$$C_{LS}^{Mo} = C_{bulk}^{Mo}/x\left[p + (1-p)D_{SS/LS}^{Mo}\right] + (1-x)\left[D_{LM/LS}^{Mo}\right] \quad (9)$$

Where x is the fraction of silicate, p is the fraction of molten silicate, C_{bulk}^{Mo} is the bulk concentration of Mo, C_{LS}^{Mo} is the concentration of Mo in the liquid silicate, $D_{SS/LS}^{Mo}$ is the partition coefficient between solid silicate and liquid silicate, and $D_{LM/LS}^{Mo}$ (= D(M) here) is the partition coefficient between liquid metal and liquid silicate (Righter et al., 1997). For Earth calculations, $x = 0.68$, and $p = 0.6$; $D_{LM/LS}^{Mo}$ is calculated using equation (8) and the regression coefficients in Table S6, and $D_{SS/LS}^{Mo}$ is $\ll 1$ for Mo (e.g., Sharp et al., 2015). $\ln D'$(Mo) is calculated first, and then converted to $\ln D$(Mo) with activity correction using metal compositions of core forming metal used in accretion calculations described above.

Calculated D(Mo) and concentrations of Mo in the Earth's magma ocean during accretion are shown in Fig. 8 compared to the values measured in the bulk silicate Earth (BSE). During most of accretion, the mantle Mo contents stay low, but continuously increase due to pressure effects and the increasing solubility of Si in the core forming Fe metal. In the "reduced to oxidized" scenario, the increasing fO_2 also causes D(Mo) to decrease and thus the Mo concentration in the mantle to increase during accretion. These calculations show that the concentration of the moderately siderophile element Mo can be explained by a rather simple scenario of continuous accretion leading to a high PT metal–silicate scenario that establishes the Mo content of Earth's PUM near the end of accretion. These results are not strongly dependent upon the fO_2 during accretion, although the "reduced to oxidized" scenario modeled here allows attainment of PUM levels of Mo at slightly lower pressures compared to the "constant fO_2" scenario. Addition of oxygen to the modeling results in negligible differences because at these PT conditions the amount of oxygen dissolved in metallic liquid is very small (Ricolleau et al., 2011), and the effect of O on the Mo activity coefficient is nearly zero ($\varepsilon_{Mo}^{Si} = 22$ vs. $\varepsilon_{Mo}^{O} = 1.26$; Steelmaking, 1988); the most important light element affecting the activity of Mo in metallic liquids is Si, as demonstrated here and by Tuff et al. (2011) and Ono-Nakazato et al. (2007).

6.3. Mo contents in a late impact scenario

A fundamental aspect of planet formation is large-scale late impacts. It is not clear if there is chemical equilibrium in a late impact scenario and this question is currently under consideration. Our new results for Mo can be used to evaluate late impact scenarios involving full and partial equilibrium, using the approach of Dauphas et al. (2014). Considering an impactor and proto-Earth merging in a late collision can be modeled using the approach and equations (11) to (15) from Dauphas et al. (2014) in which a differentiated impactor (core and mantle) impacts a differentiated proto-Earth (core and mantle) with a mass ratio of 0.5 (impactor contribution to Earth's mantle) and core fractions of 0.3 in both. We set the Mo contents of the mantle of the impactor and proto-Earth at 12 and 18 ppb, respectively, and [Mo] in core of 3200 and 3000 ppb, respectively. This results in bulk Mo of 1000 ppb for each body and D(metal/silicate) of 267 and 167 for the impactor and proto-Earth, respectively. If these bodies completely re-equilibrate, the resulting Earth mantle has a Mo content of 25.6 (Fig. 9). This is very close to the value determined by Greber et al. (2015) or 23(±7) ppb. If the mass ratio of 0.1 (impactor contribution to Earth's mantle) is used instead, the value changes slightly to 25.0 ppb. Similarly, if the mass fraction of impactor core equilibrating with Earth's mantle is 0.5 instead of 1, the value is 25.4 ppb, not much different. If however, the degree of equilibration is lowered to <0.05, the value drops below 20 ppb. However, this value is much lower than any modeling currently predicts (Rubie et al., 2015) and so for scenarios of dis-equilibrium, the value in Earth's mantle is similar to that for equilibrium and overlaps with the measured Mo content of the PUM.

Thus, producing the bulk Mo content does not necessarily require late (post-core formation) addition of chondritic materials, as some have argued for W isotopes, HSEs, and volatile elements (e.g., Touboul et al., 2015; Walker, 2009; Rose-Weston et al., 2009; Ballhaus et al., 2013). In fact, our results are consistent with the

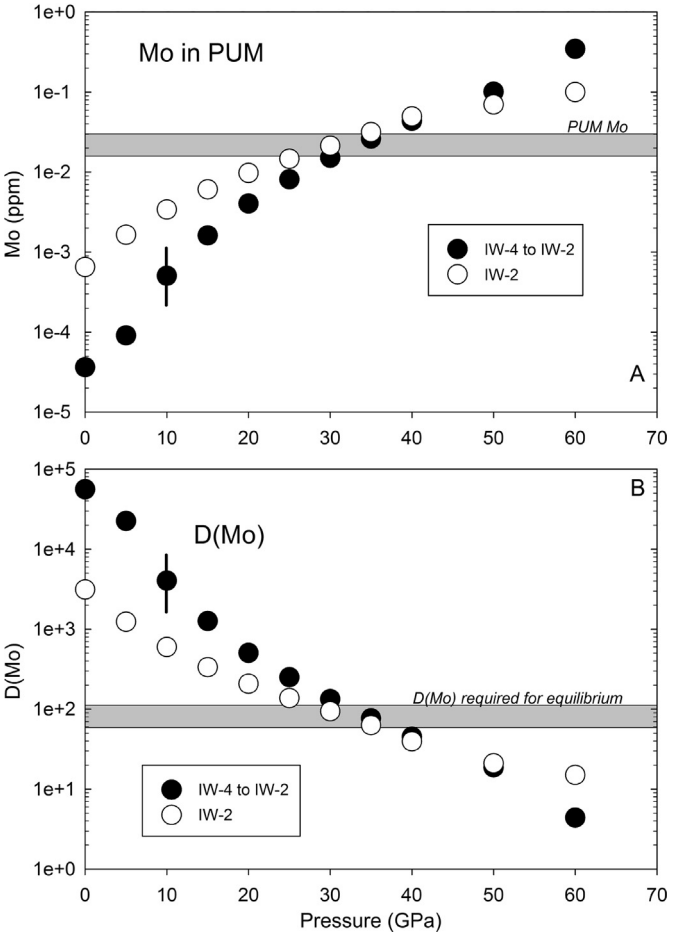

Fig. 8. (a) Calculations of mantle Mo content as Earth grows during accretion, for two different fO_2 paths. Open circles indicate a scenario with fO_2 staying relatively constant during accretion, whereas closed symbols indicate a second scenario where fO_2 increases from IW−4 to IW−2 during accretion, with the metallic liquids changing in composition as indicated in Fig. 7. (b) Calculated D(Mo) metal/silicate during accretion for increasing fO_2, and constant relative fO_2, as described for (a) and in the text. Mo content of the mantle is calculated using Equations (8) and (9). Shaded box shows the Mo content estimated for Earth's primitive upper mantle and the required range of D(Mo) to explain Mo content of the PUM (from Greber et al., 2015). All calculations are along the peridotite liquidus defined by Andrault et al. (2011). Error on D(Mo) and Mo content is propagated from the error on the regression from Table S6.

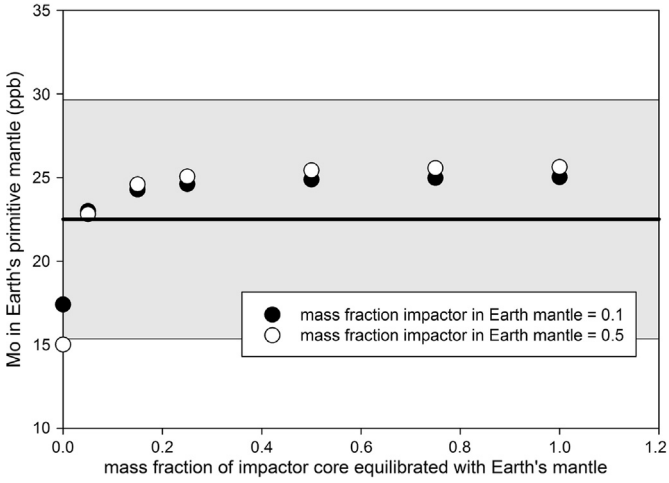

Fig. 9. Mo content of the Earth's mantle calculated for a giant impact involving the impactor and proto-Earth. Solid circles show an example where the mass fraction of the impactor in Earth's mantle is 0.12, and the open circles are where the mass fraction of the impactor in Earth's mantle is 0.5. *X*-axis shows the mass fraction of the impactor core that equilibrates with Earth's mantle. Calculations utilize equations (11) to (15) from Dauphas et al. (2014) as explained in the text.

conclusions of Greber et al. (2015) who argued that the similarity of Mo isotope composition (δ^{98}Mo) between Earth's PUM and chondritic meteorites (Hin et al., 2013) implies overall chemical and isotopic equilibrium between core and mantle.

7. Conclusions

New XANES measurements of Mo valence at high PT conditions and FeO bearing silicate melts show that Mo^{4+} is stable at high PT and below IW−1 and thus at the conditions of terrestrial core formation. Pressure has a slight but important effect on Mo partitioning causing a reduction at higher pressures; our new data double the number of experimental determination at pressures >10 GPa. Si alloyed in Fe metallic liquids causes a lower D(Mo) metal–silicate, with the most significant effect in C-bearing metallic liquids. Combination of our new data with previous experimental studies allows derivation of predictive expression for D(Mo) metal/silicate. Using our XANES results as a guide we utilize only experiments at IW−1 or lower where Mo^{4+} is stable. Using this new expression, we show that the Mo content of Earth's primitive upper mantle can be explained by chemical and (isotopic) equilibrium between core-forming metallic liquid and molten mantle in a deep magma ocean scenario (35 to 45 GPa). Future efforts should focus on obtaining partitioning data at pressures >20 GPa.

Acknowledgements

Roger Harrington provided beautiful thin sections of several experimental run products. Portions of this work were performed at GeoSoilEnviroCARS (Sector 13), Advanced Photon Source (APS), Argonne National Laboratory. GeoSoilEnviroCARS is supported by the National Science Foundation – Earth Sciences (EAR-1128799) and Department of Energy – GeoSciences (DE-FG02-94ER14466). This research used resources of the Advanced Photon Source, a U.S. Department of Energy (DOE) Office of Science User Facility operated for the DOE Office of Science by Argonne National Laboratory under Contract No. DE-AC02-06CH11357. Research was also supported by an RTOP to KR from the NASA Cosmochemistry Program, and by an NSF grant to Andrew J. Campbell. We thank Nicolas Dauphas and 3 anonymous reviewers for comments that helped improve the manuscript.

Appendix A. Supplementary material

Supplementary material related to this article can be found online at http://dx.doi.org/10.1016/j.epsl.2015.12.025.

References

Agrinier, A., Lee, C.-T., 2007. Quantifying trace element disequilibria in mantle xenoliths and abyssal peridotite. Earth Planet. Sci. Lett. 257, 290–298.
Andrault, D., Bolfan-Casanova, N., Lo Nigro, G., Bouhifd, M.A., Garbarino, G., Mezouar, M., 2011. Solidus and liquidus profiles of chondritic mantle: implication for melting of the Earth across its history. Earth Planet. Sci. Lett. 304, 251–259.
Armytage, R.M.G., Georg, R.B., Savage, P.S., Williams, H.M., Halliday, A.N., 2011. Silicon isotopes in meteorites and planetary core formation. Geochim. Cosmochim. Acta 75, 3662–3676.
Badro, J., Brodholt, J.P., Piet, H., Siebert, J., Ryerson, F.J., 2015. Core formation and core composition from coupled geochemical and geophysical constraints. Proc. Natl. Acad. Sci. USA 112, 12310–12314.
Ballhaus, C., Laurenz, V., Münker, C., Fonseca, R.O., Albarède, F., Rohrbach, A., Helmy, H.M, 2013. The U/Pb ratio of the Earth's mantle—a signature of late volatile addition. Earth Planet. Sci. Lett. 362, 237–245.
Berry, A.J., O'Neill, H.St.C., 2004. A XANES determination of the oxidation state of chromium in silicate glasses. Am. Mineral. 89, 790–798.
Berthet, S., Malavergne, V., Righter, K., 2009. Evolution of Indarch (EH4 chondrite) at 1 GPa and high temperature: implications for early planetary differentiation processes. Geochim. Cosmochim. Acta 73, 6402–6420.
Boujibar, A., Andrault, D., Bouhifd, M.A., Bolfan-Casanova, N., Devidal, J.L., Trcera, N., 2014. Metal–silicate partitioning of sulphur, new experimental and thermodynamic constraints on planetary accretion. Earth Planet. Sci. Lett. 391, 42–54.
Campbell, A.J., Danielson, L., Righter, K., Seagle, C.T., Wang, Y., Prakapenka, V.B., 2009. High pressure effects on the iron–iron oxide and nickel–nickel oxide oxygen fugacity buffers. Earth Planet. Sci. Lett. 286, 556–564.
Chakrabarti, R., Jacobsen, S.B., 2010. Silicon isotopes in the inner Solar System: implications for core formation, solar nebular processes and partial melting. Geochim. Cosmochim. Acta 74, 6921–6933.
Chi, H., Dasgupta, R., Duncan, M.S., Shimizu, N., 2014. Partitioning of carbon between Fe-rich alloy melt and silicate melt in a magma ocean–implications for the abundance and origin of volatiles in Earth, Mars, and the Moon. Geochim. Cosmochim. Acta 139, 447–471.
Cottrell, E., Walter, M.J., Walker, D., 2009. Metal–silicate partitioning of tungsten at high pressure and temperature: implications for equilibrium core formation in Earth. Earth Planet. Sci. Lett. 281, 275–287.
Dasgupta, R., Chi, H., Shimizu, N., Buono, A.S., Walker, D., 2013. Carbon solution and partitioning between metallic and silicate melts in a shallow magma ocean: implications for the origin and distribution of terrestrial carbon. Geochim. Cosmochim. Acta 102, 191–212.
Dauphas, N., Burkhardt, C., Warren, P.H., Fang-Zhen, T., 2014. Geochemical arguments for an Earth-like Moon-forming impactor. Philos. Trans. R. Soc. Lond. A, Math. Phys. Eng. Sci 372, 20130244.
Dauphas, N., Poitrasson, F., Burkhardt, C., Kobayashi, H., Kurosawa, K., 2015. Planetary and meteoritic Mg/Si and δ^{30}Si variations inherited from solar nebula chemistry. Earth Planet. Sci. Lett. 427, 236–248.
Deguen, R., Landeau, M., Olson, P., 2014. Turbulent metal–silicate mixing, fragmentation, and equilibration in magma oceans. Earth Planet. Sci. Lett. 391, 274–287.
Farges, F., Siewert, R., Brown Jr., G.E., Guesdon, A., Morin, G., 2006a. Structural environments around molybdenum in silicate glasses and melts. I. Influence of composition and oxygen fugacity on the local structure of molybdenum. Can. Mineral. 44, 731–753.
Farges, F., Siewert, R., Ponader, C.W., Brown, G.E., Pichavant, M., Behrens, H., 2006b. Structural environments around molybdenum in silicate glasses and melts. II. Effect of temperature, pressure, H_2O, halogens and sulfur. Can. Mineral. 44, 755–773.
Filiberto, J., Treiman, A.H., Le, L., 2008. Crystallization experiments on a Gusev basalt composition. Meteorit. Planet. Sci. 43, 1137–1146.
Fitoussi, C., Bourdon, B., Kleine, T., Oberli, F., Reynolds, B.C., 2009. Si isotope systematics of meteorites and terrestrial peridotites: implications for Mg/Si fractionation in the solar nebula and for Si in the Earth's core. Earth Planet. Sci. Lett. 287, 77–85.
Gao, S., Liu, X., Yuan, H., Hattendorf, B., Günther, D., Chen, L., Hu, S., 2002. Determination of forty two major and trace elements in USGS and NIST SRM glasses by laser ablation-inductively coupled plasma–mass spectrometry. Geostand. Newsl. 26, 181–196.
Georg, R.B., Halliday, A.N., Schauble, E.A., Reynolds, B.C., 2007. Silicon in the Earth's core. Nature 447, 1102–1106.
Greber, N.D., Puchtel, I.S., Nägler, T.F., Mezger, K., 2015. Komatiites constrain molybdenum isotope composition of the Earth's mantle. Earth Planet. Sci. Lett. 421, 129–138.
Hillgren, V.J., Drake, M.J., Rubie, D.C., 1996. High-pressure and high-temperature metal–silicate partitioning of siderophile elements: the importance of silicate liquid composition. Geochim. Cosmochim. Acta 60, 2257–2263.

Hillgren, V.J., Gessmann, C.K., Li, J., 2000. An experimental perspective on the light element in Earth's core. In: Canup, R., Righter, K. (Eds.), Origin of the Earth and Moon. Univ. Arizona Press, Tucson, Arizona, pp. 245–263.
Hin, R.C., Burkhardt, C., Schmidt, M.W., Bourdon, B., Kleine, T., 2013. Experimental evidence for Mo isotope fractionation between metal and silicate liquids. Earth Planet. Sci. Lett. 379, 38–48.
Holzheid, A., Borisov, A., Palme, H., 1994. The effect of oxygen fugacity and temperature on solubilities of nickel, cobalt, and molybdenum in silicate melts. Geochim. Cosmochim. Acta 58, 1975–1981.
Holzheid, A., Palme, H., Chakraborty, S., 1997. The activities of NiO, CoO and FeO in silicate melts. Chem. Geol. 139, 21–38.
Jana, D., Walker, D., 1997a. The influence of silicate melt composition on distribution of siderophile elements among metal and silicate liquids. Earth Planet. Sci. Lett. 150, 463–472.
Jana, D., Walker, D., 1997b. The influence of sulfur on partitioning of siderophile elements. Geochim. Cosmochim. Acta 61, 5255–5277.
Kegler, P., Holzheid, A., Frost, D.J., Rubie, D.C., Dohmen, R., Palme, H., 2008. New Ni and Co metal–silicate partitioning data and their relevance for an early terrestrial magma ocean. Earth Planet. Sci. Lett. 268, 28–40.
Kendall, J., Melosh, H.J., 2014. Dispersion of planetesimal iron cores during accretional impacts. In: Lunar and Planetary Science Conference, vol. 45, p. 2827.
Lewis, R.D., Lofgren, G.E., Franzen, H.F., Windom, K.E., 1993. The effect of Na vapor on the Na content of chondrules. Meteoritics 28, 622–628.
Ma, Z., 2001. Thermodynamic description for concentrated metallic solutions using interaction parameters. Metall. Mater. Trans., B 32, 87–103.
Malavergne, V., Charon, E., Jones, J., Cordier, P., Righter, K., Deldicque, D., Hennet, L., 2016. The formation of nuggets of highly siderophile elements in quenched silicate melts at high temperatures: before or during the silicate quench? Earth Planet. Sci. Lett. 434, 197–207.
McDonough, W.F., 2003. Compositional model for the Earth's core. Treatise Geochem. 2, 547–568.
Newsom, H.E., 1995. Global Earth Physics: A Handbook of Physical Constants. In: AGU Reference Shelf, vol. 1, pp. 159–189.
O'Neill, H.St.C, Eggins, S.M., 2002. The effect of melt composition on trace element partitioning: an experimental investigation of the activity coefficients of FeO, NiO, CoO, MoO_2 and MoO_3 in silicate melts. Chem. Geol. 186, 151–181.
Ono-Nakazato, H., Taguchi, K., Maruo, R., Usui, T., 2007. Silicon deoxidation equilibrium of molten Fe–Mo alloy. ISIJ Int. 47, 365–369.
Poe, B.T., Romano, C., Zotov, N., Cibin, G., Marcelli, A., 2001. Compression mechanisms in aluminosilicate melts: Raman and XANES spectroscopy of glasses quenched from pressures up to 10 GPa. Chem. Geol. 174, 21–31.
Ravel, B., Newville, M., 2005. ATHENA, ARTEMIS, HEPHAESTUS: data analysis for X-ray absorption spectroscopy using IFEFFIT. J. Synchrotron Radiat. 12, 537–541.
Ricolleau, A., Fei, Y., Corgne, A., Siebert, J., Badro, J., 2011. Oxygen and silicon contents of Earth's core from high pressure metal–silicate partitioning experiments. Earth Planet. Sci. Lett. 310, 409–421.
Righter, K., 2011. Prediction of metal–silicate partition coefficients for siderophile elements: an update and assessment of PT conditions for metal–silicate equilibrium during accretion of the Earth. Earth Planet. Sci. Lett. 304, 158–167.
Righter, K., Drake, M.J., 1999. Effect of water on metal–silicate partitioning of siderophile elements: a high pressure and temperature terrestrial magma ocean and core formation. Earth Planet. Sci. Lett. 171, 383–399.
Righter, K., Drake, M.J., 2000. Metal/silicate equilibrium in the early Earth—new constraints from the volatile moderately siderophile elements Ga, Cu, P, and Sn. Geochim. Cosmochim. Acta 64, 3581–3597.
Righter, K., Ghiorso, M.S., 2012. Redox systematics of a magma ocean with variable pressure–temperature gradients and composition. Proc. Natl. Acad. Sci. USA 109, 11955–11960.
Righter, K., Drake, M.J., Yaxley, G., 1997. Prediction of siderophile element metal–silicate partition coefficients to 20 GPa and 2800 °C: the effect of pressure, temperature, fO_2 and silicate and metallic melt composition. Phys. Earth Planet. Inter. 100, 115–134.
Righter, K., Hervig, R.L., Kring, D., 1998. Accretion and core formation in Mars: molybdenum contents of melt inclusion glasses from three SNC meteorites. Geochim. Cosmochim. Acta 62, 2167–2177.
Righter, K., Sutton, S.R., Newville, M., Le, L., Schwandt, C.S., Uchida, H., Lavina, B., Downs, R.T., 2006. Oxidation state of vanadium in spinel and silicate melt: implications for planetary basalts and mantle melting. Am. Mineral. 91, 1643–1656.
Righter, K., Humayun, M., Danielson, L.R., 2008. High pressure and temperature partitioning of palladium during core formation. Nat. Geosci. 1, 321–323.
Righter, K., Pando, K., Danielson, L.R., Lee, C.-T., 2010. Partitioning of Mo, P and other siderophile elements (Cu, Ga, Sn, Ni, Co, Cr, Mn, V, W) between metal and silicate melt as a function of temperature and melt composition. Earth Planet. Sci. Lett. 291, 1–9.
Righter, K., Danielson, L.R., Pando, K., Morris, R.V., Graff, T.G., Agresti, D.G., Martin, A.M., Sutton, S.R., Newville, M., Lanzirotti, A., 2013. Redox systematics of martian magmas with implications for magnetite stability. Am. Mineral. 98, 616–628.
Rose-Weston, L., Brenan, J.M., Fei, Y., Secco, R.A., Frost, D.J., 2009. Effect of pressure, temperature, and oxygen fugacity on the metal–silicate partitioning of Te, Se, and S: implications for Earth differentiation. Geochim. Cosmochim. Acta 73, 4598–4615.
Rubie, D.C., Frost, D.J., Mann, U., Asahara, Y., Nimmo, F., Tsuno, K., Kegler, P., Holzheid, A., Palme, H., 2011. Heterogeneous accretion, composition and core–mantle differentiation of the Earth. Earth Planet. Sci. Lett. 301, 31–42.
Rubie, D.C., Jacobson, S.A., Morbidelli, A., O'Brien, D.P., Young, E.D., de Vries, J., Frost, D.J., 2015. Accretion and differentiation of the terrestrial planets with implications for the compositions of early-formed Solar System bodies and accretion of water. Icarus 248, 89–108.
Rudnick, R.L., Gao, S., Ling, W., Liu, Y., McDonough, W.F., 2004. Petrology and geochemistry of spinel peridotite xenoliths from the Hannuoba and Qixia, North China craton. Lithos 77, 609–637.
Sanloup, C., Drewitt, J.W., Konôpková, Z., Dalladay-Simpson, P., Morton, D.M., Rai, N., Morgenroth, W., 2013. Structural change in molten basalt at deep mantle conditions. Nature 503, 104–107.
Savage, P.S., Moynier, F., 2013. Silicon isotopic variation in enstatite meteorites: clues to their origin and Earth-forming material. Earth Planet. Sci. Lett. 361, 487–496.
Shahar, A., Ziegler, K., Young, E.D., Ricolleau, A., Schauble, E.A., Fei, Y., 2009. Experimentally determined Si isotope fractionation between silicate and Fe metal and implications for Earth's core formation. Earth Planet. Sci. Lett. 288, 228–234.
Sharp, M., Righter, K., Walker, R.J., 2015. Estimation of trace element concentrations in the lunar magma ocean using mineral- and metal–silicate melt partition coefficients. Meteorit. Planet. Sci. 50, 733–758.
Shofner, G.A., 2011. High pressure redox geochemistry of tungsten in metal–silicate systems: implications for core formation in the Earth. Ph.D. thesis. University of Maryland, 175 pp.
Siebert, J., Badro, J., Antonangeli, D., Ryerson, F.J., 2013. Terrestrial accretion under oxidizing conditions. Science 339, 1194–1197.
Siebert, J., Corgne, A., Ryerson, F.J., 2011. Systematics of metal–silicate partitioning for many siderophile elements applied to Earth's core formation. Geochim. Cosmochim. Acta 75, 1451–1489.
Steelmaking, J., 1988. Steelmaking Data Sourcebook. Gordon and Breach Science Publishers, Montreux.
Sutton, S.R., Bertsch, P.M., Newville, M., Rivers, M.L., Lanzirotti, A., Eng, P., 2002. Microfluoresence and microtomography analyses of heterogeneous Earth and environmental materials (in applications of synchrotron radiation in low-temperature geochemistry and environmental sciences). Rev. Mineral. Geochem. 49, 429–483.
Touboul, M., Puchtel, I.S., Walker, R.J., 2015. Tungsten isotopic evidence for disproportional late accretion to the Earth and Moon. Nature 520, 530–533.
Tuff, J., Wood, B.J., Wade, J., 2011. The effect of Si on metal–silicate partitioning of siderophile elements and implications for the conditions of core formation. Geochim. Cosmochim. Acta 75, 673–690.
Wade, J., Wood, B.J., 2001. The Earth's 'missing' niobium may be in the core. Nature 409, 75–78.
Wade, J., Wood, B.J., 2005. Core formation and the oxidation state of the Earth. Earth Planet. Sci. Lett. 236, 78–95.
Wade, J., Wood, B.J., Tuff, J., 2012. Metal–silicate partitioning of Mo and W at high pressures and temperatures: evidence for late accretion of sulphur to the Earth. Geochim. Cosmochim. Acta 85, 57–74.
Wagner, C., 1962. Thermodynamics of Alloys. Addison–Wesley, Reading, MA.
Walker, R.J., 2009. Highly siderophile elements in the Earth, Moon and Mars: update and implications for planetary accretion and differentiation. Chem. Erde Geochem. 69, 101–125.
Walter, M.J., Thibault, Y., 1995. Partitioning of tungsten and molybdenum between metallic liquid and silicate melt. Science 270, 1186–1189.
Wood, B.J., Walter, M.J., Wade, J., 2006. Accretion of the Earth and segregation of its core. Nature 441, 825–833.
Wood, B.J., Kiseeva, E.S., Mirolo, F.J., 2014. Accretion and core formation: the effects of sulfur on metal–silicate partition coefficients. Geochim. Cosmochim. Acta 145, 248–267.
Ziegler, K., Young, E.D., Schauble, E.A., Wasson, J.T., 2010. Metal–silicate silicon isotope fractionation in enstatite meteorites and constraints on Earth's core formation. Earth Planet. Sci. Lett. 295, 487–496.